Applied Energy 260 (2020) 114134

Contents lists available at ScienceDirect

Applied Energy

journal homepage: www.elsevier.com/locate/apenergy

Bi-level optimal sizing and energy management of hybrid electric propulsion systems

Jianyun Zhu, Li Chen*, Xuefeng Wang, Long Yu

State Key Laboratory of Ocean Engineering, Institute of Power Plant and Automation, Shanghai Jiao Tong University, China

HIGHLIGHTS

- A bi-level method is proposed for the optimization of a hybrid electric propulsion system.
- Optimal component sizing and energy management are implemented simultaneously.
- A modified adaptive equivalent consumption minimization strategy is developed.
- The proposed bi-level method outperforms single-level optimizations.

ARTICLE INFO

Keywords:
Multiobjective bi-level optimization
Hybrid electric propulsion system
Modified adaptive equivalent consumption minimization strategy
Fuel consumption
Greenhouse gas emission
Net present cost

ABSTRACT

Hybrid electric propulsion systems attract considerable research interest because of their potential to reduce fuel consumption, greenhouse gas emission, and net present cost. However, independent optimization for component sizing or energy management may lead to performance degradation. The present study proposes a multiobjective bi-level optimization that performs component sizing at the upper level and energy management at the lower level simultaneously. Multiobjective particle swarm optimization is developed for the upper level because of its merits in computational time and generational distance. An adaptive equivalent consumption minimization strategy, which has a light computational load, has been modified for the lower level by updating the equivalence factor based on the battery stage of charge and engine efficiency. Real-time hardware-in-the-loop experiments are carried out to validate the effectiveness of the optimization. The results of the proposed bi-level optimization are compared with two independent single-level optimizations. The optimal solution of the proposed method is significantly superior to the single-level optimizations. Furthermore, the result of the single-lower-level optimization is closer to that of the bi-level optimization than that of the single-upper-level optimization.

1. Introduction

As stringent emission legislations have been enacted on the shipping industry, hybrid electric propulsion systems (HEPSs) have attracted considerable interest from several academic institutions and industries because of their potential to reduce fuel consumption, greenhouse gas (GHG) emissions, and cost [1,2]. In HEPSs, with the help of motors and power electronics, diesel engines can function in high efficiency areas by charging and discharging batteries under dynamic operating conditions. The performance of an HEPS is mainly determined by two levels of operation [3,4]. One, known as the upper level, is the component sizing of engine displacement, motor diameter, battery capacity, and others, which should be carefully designed before manufacturing an HEPS [3,5]. The other, known as the lower level, is the multi-energy management that must be carefully controlled during operation after manufacturing the HEPS [4,6]. Therefore, the ideal performance of the HEPS can be achieved with optimal component sizing and energy management strategy during the operation. This study focuses on bi-level optimization considering component sizing and energy management simultaneously for HEPSs.

The previous study on the performance improvement of HEPSs can be mainly classified into two categories, which consider one of the two levels. The first category uses optimal design methods to determine component sizes in terms of one or more of the three objectives (minimum fuel consumption, GHG emission, and cost) but ignores the optimization of energy management. For example, a genetic algorithm [3], two heuristic criteria [7], particle swarm optimization [8], and non-dominated sorting genetic algorithm II [9] were developed to

* Corresponding address at: Mulan Building B629, Shanghai Jiao Tong University, 800 Dong Chuan Rd., Shanghai 200240, China.
E-mail address: li.h.chen@sjtu.edu.cn (L. Chen).

https://doi.org/10.1016/j.apenergy.2019.114134
Received 1 August 2019; Received in revised form 19 October 2019; Accepted 11 November 2019

Nomenclature

Abbreviations

AECMS	adaptive equivalent consumption minimization strategy
DG	diesel generator
DP	dynamic programming
ESS	energy storage system
GA	genetic algorithm
GHG	greenhouse gas
HEPS	hybrid electric propulsion systems
MAECMS	modified adaptive equivalent consumption minimization strategy
MOPSO	multiobjective particle swarm optimization
NPC	net present cost
NSGA-II	non-dominated sorting genetic algorithm
PSO	particle swarm optimization
SOC	stage of charge

Symbols

A_e/A_o	blade–area ratio
C_{air}	air resistance coefficient
C_F	frictional resistance coefficient
C_W	wave-making resistance coefficient
c_{bat}	unit cost per capacity of ESS ($/kWh)
c_{DG}	unit cost of DG ($/kW)
c_{fuel}	unit cost of diesel fuel ($/kg)
c_M	unit cost of motor ($/W)
c_{sho}	unit cost of shore electricity ($/kWh)
D	propeller diameter (m)
D_{i+}	distance from point i in the Pareto solution set to the ideal point
D_{i-}	distance from point i in the Pareto solution set to the nadir point
d_M	diameter of motor rotor (m)
E_{sho}	consumed shore electricity (kWh)
e_{Dk}	Willans line coefficients of diesel engine (k = *00*, *01*, *02*, *10*, *11*, *loss0*, *loss2*)
e_{Mk}	Willans line coefficients of motor (k = *00*, *01*, *02*, *10*, *11*, *loss0*, *loss2*)
F_{ij}	j^{th} objective of point i
g_{bat}	annual inflation rate of the acquisition cost of battery
g_{fuel}	annual inflation rate of diesel fuel
g_{sho}	annual inflation rate of shore electricity
H_{LHV}	lower heating value of diesel fuel (J/kg)
I	annual interest rate
I_{bat}	output current of battery cell (A)
$I_{bat\_\max}$	maximum current of charging (A)
$I_{bat\_\min}$	minimum current of discharging (A)
I_{ele}	life cycle average GHG intensity of shore electricity (kg/kWh)
I_{fuel}	life cycle average GHG intensity of diesel fuel (kg/kg)
i	gear ratio of gearbox
J	advance coefficient of propeller
K_T	thrust coefficient of propeller
K_Q	torque coefficient of propeller
l_M	length of the rotor (m)
m	mass of ship (kg)
$\dot{m}_f$	mass flow of diesel fuel (kg/s)
n_{rep}	total number of battery replacements during service life
m_{su}	fuel consumption of DG per startup (kg)
$\dot{m}_{vir}$	virtual fuel consumption rate (kg/s)
N_{ESS}	net present cost of battery replacement ($)
N_{ini}	net present cost of initial equipment investment ($)
N_{ope}	net present cost of system operation ($)
n	propeller speed (r/min)
n_{ESS}	number of battery modules in ESS
n_{su}	number of DG startup times
P/D	pitch ratio
P_{aux}	auxiliary load (W)
P_{bat}	terminal power of battery cell (W)
P_D	output power of diesel engine (kW)
P_{DG_rate}	rated power of DG (kW)
P_{ESS}	output power of ESS (kW)
$P_{hot}(t)$	hotel load (kW)
$P_M(t)$	output power of motor (kW)
P_{M_in}	input power of motor (kW)
P_{M_rate}	rated power of motor (kW)
P_{pro}	propulsive load (kW)
P_{req}	total power requirement (kW)
P_{ser}	service load (kW)
p_{Da}	available mean effective pressure of diesel engine (Pa)
p_{De}	mean effective pressure of diesel engine (Pa)
p_{Dloss}	mean effective pressure loss of diesel engine (Pa)
p_{Ma}	available mean effective pressure of motor (Pa)
p_{Me}	mean effective pressure of motor (Pa)
p_{Mloss}	equivalent mean effective pressure loss of motor (Pa)
Q	torque of one propeller (Nm)
Q_{bat}	battery cell capacity (Ah)
Q_{ESS}	ESS capacity (Ah)
R_{Air}	air resistance (N)
R_{bat}	internal resistance of battery cell (Ω)
R_F	frictional resistance (N)
R_i	distance index
R_{total}	ship resistance (N)
R_W	wave-making resistance (N)
s	equivalence factor of virtual fuel consumption
S_{air}	advance facing area of the ship in the air (m^2)
S_G	on/off state factor of generator
S_{hull}	wet-surface area of hull (m^2)
s_{ij}	j-th objective of point i after non-dimensionalization
T	effective thrust of one propeller (N)
T_D	output torque of diesel engine (Nm)
T_M	output torque of motor (Nm)
t_1	thrust deduction coefficient
t_{DG}	startup time limitation of DG (s)
t_{count}	time duration considered in the calculation of fuel consumption (s)
V_{bat}	open-circuit voltage of battery cell (V)
V_D	engine cylinder displacement (m^3)
V_M	volume of motor rotor (m^3)
v	velocity of ship (m/s)
v_D	average velocity of piston (m/s)
v_M	velocity of a point at the rotor surface (m/s)
$v_{\max}$	maximum speed of ship (m/s)
v_{req}	peed requirement (m/s)
$\mathbf{x}$	optimization parameter set
$\mathbf{x}_E$	subset of energy management parameters
$\mathbf{x}_S$	subset of sizing parameters
Y	lifetime of ship (year)
Y_{ESS}	lifetime of lithium-ion battery (year)
Z	number of propeller blades

Greek symbols

Δc_{gen}	correction factor accounting for electrical components
η_{colm}	Coulombic efficiency
$\bar{\eta}_{\text{DGs}}(k)$	average efficiency of DGs
$\eta_G(t)$	efficiency of generator

η_{G0}	base efficiency of generator	$\omega_D(t)$	angular velocity of diesel engine (rad/s)
η_{Gb}	efficiency of gearbox	$\omega_M(t)$	angular velocity of motor (rad/s)
$\eta_M(t)$	efficiency of motor	ρ	seawater density (kg/m^3)
$\lambda(t)$	ratio of generator power to its rated power		

select the size of components of HEPSs. In this category, because of simplicity, rule-based energy management strategies with static parameters are used. Therefore, the performance of the optimal solution is rather limited. Moreover, the optimal solution does not necessarily achieve optimal performance, even with other advanced energy management strategies.

The second category is to use optimal or near-optimal strategies to manipulate energy flow management during operation aiming to achieve minimum fuel consumption, though, for HEPSs with predefined sizes. For example, model predictive control [4], fuzzy-based particle swarm optimization [6], equivalent cost minimization strategy [10], and stochastic energy management strategy [11] were applied to HEPSs. However, the predefined sizes may not be optimized. When the sizes change, the constraints of the optimal energy management change; thereafter, the optimal solution for energy management will change accordingly.

In spite of the increasing number of studies on HEPSs, the optimization of HEPSs synchronously considering component sizing and energy management, to the best of our knowledge, has not been reported yet. Unfortunately, independent optimization for component sizing or energy management may lead to performance degradation. Therefore, this study proposes a bi-level optimization framework to integrate component sizing (upper level) and energy management (lower level) into a single algorithm for HEPSs. The bi-level optimization has exhibited advantages over single-level optimizations in the planning and development of an islanded microgrid [12], a stand-alone hybrid power system [13], and a hybrid electric vehicle [14,15]. Nevertheless, significant differences are observed between the HEPSs and those systems. For example, comparing HEPS ships with hybrid electric vehicles, long-range and durable endurance is essential for the former, whereas the latter can be refilled, recharged, or conveniently repaired. Moreover, HEPS vessels use multiple gensets or multiple types of prime movers that are connected to a common power bus and independently controlled, whereas hybrid vehicles use a set of power devices. In addition, HEPS vessels typically can sail for a long time on a relatively stable power, and it is inefficient to apply regenerative braking technology because of the lack of direct adhesion between the propeller and the water, in contrast to hybrid vehicles that are likely to stop-and-go frequently.

The bi-level optimization, which relies on an integrated algorithm, was more complex than the traditional independent single-level algorithms. The contradiction between the effectiveness to obtain an optimal solution and computational load is more significant for the integrated algorithm. Thus, the selection of the algorithms for the upper and lower levels is significant.

Regarding the multiobjective optimization of the size of components at the upper level, there are alternative approaches for design space exploration. One class of approaches aggregates the objectives into a single-objective formulation by introducing weighting factors. Then, the problem is solved by single-objective optimization tools, such as the Newton–Raphson method [16] and response surface method [17]. The drawback is that inappropriate weighting factors can deteriorate the optimization performance; thereafter, the selection of the weighting factors becomes a challenge. To overcome this drawback, Pareto-based approaches such as multiobjective ant colony optimization (MOACO) [18], non-dominated sorting genetic algorithm II (NSGA-II) [19], and multiobjective particle swarm optimization (MOPSO) [20] have been applied. MOACO has the problem of premature convergence [21]. The comparison between MOPSO and NSGA-II showed that MOPSO outperforms NSGA-II in terms of computational time and generational distance in most cases [22]. Therefore, in this study, MOPSO has been selected for component sizing optimization at the upper level.

For optimal control of energy management at the lower level, dynamic programming (DP) [15], multiobjective electromagnetism-like algorithm [23] and simulated annealing method [24] have been developed to obtain a global optimal energy management schedule. However, because of the heavy computational load, these global optimization approaches cannot be directly used for high-efficiency applications in real time [25]. As a result, rule-based control approaches (abstracted from the optimization results with DP algorithm) [26–28], driving cycle analysis [29], model predictive control [4,30], and equivalent consumption minimization strategy (ECMS) [31] have been explored. Among them, ECMS, initially introduced in 1999 [32], has the potential to reduce computational complexity by transforming the global optimization problem into a local (instantaneous) problem based on Pontryagin's minimum principle [33]. A key feature that determines the effectiveness of ECMS is the equivalence factor of the electrical energy with respect to the fossil energy, which is affected by the efficiency of diesel engines, batteries, and related energy flows. Instead of setting the equivalence factor as a constant as per previous studies [32,34], adaptive ECMSs have been recently proposed to automatically tune the equivalence factor according to the stage of charge (SOC) of the battery [35] under predicted driving cycles [36] and recognized driving patterns [37]. To compensate for the lack of consideration of engine efficiency, this paper proposes a modified adaptive ECMS (MAECMS), which can update the equivalence factor based on the instantaneous efficiency of the battery and the engine.

The bi-level multiobjective optimization method proposed in this paper consists of MOPSO for component sizing at the upper level and MAECMS for energy management at the lower level. The optimization problem considers three optimization objectives: fuel consumption, GHG emission, and net present cost (NPC). The effectiveness of the proposed method is demonstrated by considering an HEPS of an anchor-handling tug supply (AHTS) vessel. The independent optimizations at the upper and lower levels, named single-upper-level and single-lower-level optimizations, respectively, are performed to highlight the significance of the proposed method. The performance is verified by hardware-in-the-loop (HIL) experiments.

The major contributions can be summarized as follows: (1) The bi-level multiobjective optimization framework has been proposed for the design of HEPSs. The framework simultaneously addresses component sizing and energy management, which were independently optimized in the existing literature despite the deep interrelationship between them. (2) MAECMS, which can efficiently achieve a local optimum solution with reduced computational load, is developed for the lower-level implementation of bi-level optimization. The MAECMS can improve the traditional AECMS by adaptively adjusting the equivalence factor according to the instantaneous operation of the battery and diesel engines. (3) HIL experiments are conducted to validate the effectiveness of the proposed method.

The rest of the paper is organized as follows: the description and modeling of the HEPS are detailed in Section 2. The optimization problem has been formulated in Section 3. Section 4 demonstrates the bi-level optimization method. Results have been discussed in Section 5. Finally, Section 6 concludes the article.

2. System description and modeling

Fig. 1 shows a twin-screw HEPS. There are two identical propellers; each is driven by a motor through a gearbox. There are two identical generators; each runs on a diesel engine. Generators and motors share a power bus with the energy storage system (ESS) and the shore power connection. In addition, hotel and service loads consume electricity from the power bus.

2.1. Ship dynamics

The longitudinal dynamics of a twin-screw ship is given by [38,39]:

$$m\frac{\mathrm{d}v}{\mathrm{d}t} = 2(1-t_1)\cdot T(t) - R_{total}(t) \tag{1}$$

where m is the mass of the ship, v is the velocity of the ship, t_1 is the thrust deduction coefficient, $T(t)$ is the thrust, and $R_{total}(t)$ is the ship resistance.

2.1.1. Resistance

The ship resistance includes frictional resistance $R_F(t)$, wave-making resistance $R_W(t)$, and air resistance $R_{Air}(t)$ [39,40].

$$R_{total}(t) = R_F(t) + R_W(t) + R_{Air}(t) \tag{2}$$

$$R_F(t) = \frac{1}{2}C_F\rho S_{hull}\cdot v^2(t) \tag{3}$$

$$R_W(t) = \frac{1}{2}C_W\rho S_{hull}\cdot v^2(t) \quad \text{and} \tag{4}$$

$$R_{Air}(t) = \frac{1}{2}C_{Air}\rho S_{Air}\cdot v^2(t) \tag{5}$$

where C_{air} is the air resistance coefficient, C_F is the frictional resistance coefficient, C_W is the wave-making resistance coefficient, ρ is the sea-water density, S is the wet-surface area of the hull, and S_{air} is the advance facing area of the ship in the air.

2.1.2. Propellers

The two propellers are identical. For each propeller, the mathematical models of the thrust $T(t)$ and the torque $Q(t)$ are given below [39,40]:

$$T(t) = K_T D^4\rho\cdot n^2(t) \quad \text{and} \tag{6}$$

$$Q(t) = K_Q D^5\rho\cdot n^2(t) \tag{7}$$

where K_T is the thrust coefficient, K_Q is the torque coefficient, n is the propeller speed in r/min, and D is the propeller diameter. K_T and K_Q is given by [41,42]:

$$K_T = f_T(J(t),\ P/D,\ A_e/A_o,\ Z) \tag{8}$$

$$K_Q = f_Q(J(t),\ P/D,\ A_e/A_o,\ Z) \quad \text{and} \tag{9}$$

$$J(t) = D\cdot\frac{v(t)}{n(t)} \tag{10}$$

where $J(t)$ is the advance coefficient, P/D is the pitch ratio, A_e/A_o is the blade–area ratio, and Z is the number of propeller blades.

2.2. Gearboxes

There are two identical gearboxes. Each connects a motor and a propeller. Assuming that the mechanical loss is ignorable, the input torque of the gearbox is the same as the output torque of the motor, as well as the angular velocity and the power. The mathematical description is given below:

$$\omega_M(t) = \frac{\pi i}{30}\cdot n(t) \tag{11}$$

$$T_M(t) = \frac{1}{i\eta_{Gb}}\cdot Q(t) \quad \text{and} \tag{12}$$

$$P_M(t) = T_M(t)\cdot\omega_M(t) \tag{13}$$

where $\omega_M(t)$ is the angular velocity of the motor, $T_M(t)$ is the output torque of the motor, $P_M(t)$ is the output power of the motor, and i η_{Gb} are the gear ratio and efficiency of gearbox.

2.3. Motors

The motors are modeled based on the Willans line method [43–46]. By changing the two "size parameters," i.e., the diameter and length of the motor rotor, the Willans line method is able to establish a scalable model for a series of motors belonging to the same category. To achieve the scalability, two concepts originated from the field of internal combustion engines are introduced, namely, mean effective pressure $p_{Me}(t)$ and available mean effective pressure $p_{Ma}(t)$. Regarding the motor, $p_{Me}(t)$ can be interpreted as the ability of a unit volume of the rotor to provide torque; $p_{Ma}(t)$ represents the maximum mean effective pressure when all the consumed electrical energy is converted into mechanical energy [43].

$$p_{Me}(t) = \frac{1}{2V_M}\cdot T_M(t) \tag{14}$$

$$p_{Ma}(t) = \frac{1}{2V_M}\cdot\frac{P_{M\_in}(t)}{\omega_M(t)} \quad \text{and} \tag{15}$$

$$V_M = \pi\left(\frac{d_M}{2}\right)^2 l_M \tag{16}$$

where $P_{M\_in}(t)$ is the input power of the motor, V_M is the volume of the motor rotor, d_M is the diameter of the rotor, and l_M is the length of the rotor.

According to the Willans line method, the relationship between $p_{Me}(t)$ and $p_{Ma}(t)$ are described below [43]:

$$p_{Me}(t) = [e_{M0}(v_M) - e_{M1}(v_M)\cdot p_{Ma}(t)]\cdot p_{Ma}(t) - p_{Mloss}(v_M) \tag{17}$$

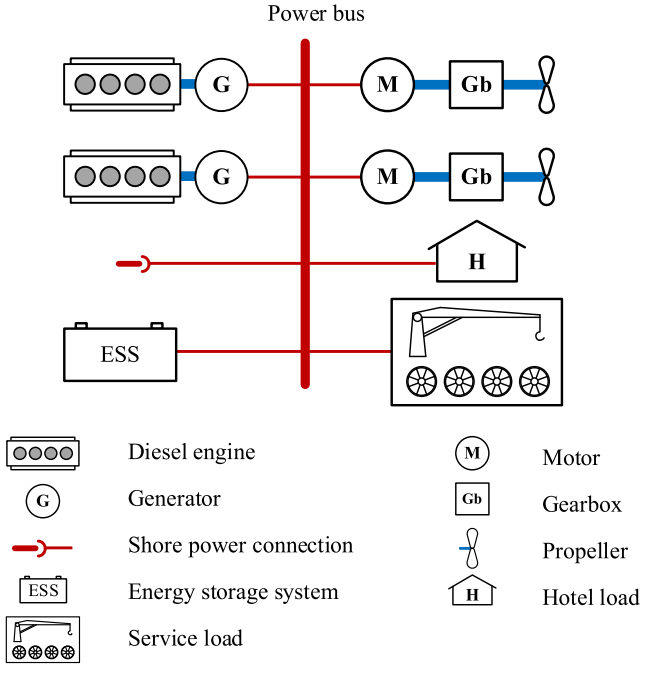

Fig. 1. Twin-screw HEPS with ESS and shore power connection.

$$e_{M0}(v_M) = e_{M00} + e_{M01}\cdot v_M(t) + e_{M02}\cdot {v_M}^2(t)$$
$$e_{M1}(v_M) = e_{M10} + e_{M11}\cdot v_M(t)$$
$$p_{Mloss}(v_M) = e_{Mloss,0}\cdot + e_{Mloss,2}\cdot {v_M}^2(t)$$
$$v_M(t) = \tfrac{1}{2} d_M\cdot\omega_M(t), \tag{18}$$

where $v_M(t)$ is the velocity of a point at the rotor surface, $p_{Mloss}(v_M)$ is the equivalent mean effective pressure loss of the motor, and e_{M00}, e_{M01}, e_{M02}, e_{M10}, e_{M11}, $e_{Mloss,0}$, and $e_{Mloss,2}$ are the Willans line coefficients that are considered to be the same for motors of the same category [43].

Therefore, the Willans line coefficients can be identified by using the data of a baseline motor. After that, the mean effective pressure $p_{Me}(t)$ of a scalable motor with new values of d_M and l_M can be calculated from (17). Substitution of (13) and (15) yields the calculation of the efficiency $\eta_M(t)$, as given below:

$$\eta_M(t) = \frac{P_M(t)}{P_{M\_in}(t)} = \frac{p_{Me}(t)}{p_{Ma}(t)} \tag{19}$$

2.4. Diesel engines

A scalable diesel engine model is established based on the Willans line method [44], which has been experimentally validated on different engines [43]. Diesel engines can be scalable, along with the key parameter, known as engine cylinder displacement. The mean effective pressure $p_{De}(t)$ and the available mean effective pressure $p_{Da}(t)$ are defined below:

$$p_{De}(t) = \frac{4\pi}{V_D}\cdot T_D(t) \tag{20}$$

$$p_{Da}(t) = 4\pi\cdot\frac{H_{LHV}}{V_D}\frac{\dot{m}_f(t)}{\omega_D(t)} \quad \text{and} \tag{21}$$

$$V_D = S_D\cdot\pi\left(\frac{B_D}{2}\right)^2 \tag{22}$$

where V_D is the engine cylinder displacement; $T_D(t)$, $\omega_D(t)$, B_D, and S_D are the output torque, angular velocity, bore, and stroke of the diesel engine, respectively; H_{LHV} is the lower heating value of the diesel fuel; and $\dot{m}_f(t)$ is the mass flow of the diesel fuel.

Similar to the modeling of motors, the relationship between the mean effective pressure and the available mean effective pressure of the diesel engine can be expressed as follows:

$$p_{De}(t) = [e_{D0}(v_M) - e_{D1}(v_M)\cdot p_{Da}]\cdot p_{Da}(t) - p_{Dloss}(v_M) \tag{23}$$

$$e_{D0}(v_M) = e_{D00} + e_{D01}\cdot v_D(t) + e_{D02}\cdot v_D^2(t)$$
$$e_{D1}(v_M) = e_{D10} + e_{D11}\cdot v_D(t)$$
$$p_{Dloss}(v_M) = e_{Dloss,0}\cdot + e_{Dloss,2}\cdot v_D^2(t)$$
$$v_D(t) = \tfrac{S_D}{\pi}\cdot\omega_D(t), \tag{24}$$

where $p_{Dloss}(t)$ is the mean effective pressure loss of the diesel engine and $v_D(t)$ is the average velocity of the piston. The Willans line coefficients, e_{D00}, e_{D01}, e_{D02}, e_{D10}, e_{D11}, $e_{Dloss,0}$, and $e_{Dloss,2}$, are considered to be constants for diesel engines belonging to the same category [43].

The Willans line coefficients can be identified by using data of a baseline diesel engine. With $T_D(t)$ and V_D, the mean effective pressure $p_{De}(t)$ can be calculated from (20). After that, the available mean effective pressure $p_{Da}(t)$ of a newly designed engine can be calculated from (23). Then, the mass flow $\dot{m}_f$ can be obtained from (21).

2.5. Generators

Two identical brushless synchronous generators run on two diesel engines. A generator is combined with a diesel engine to form a diesel generator (DG). The specifications of the generator should match those of the corresponding diesel engine. For each generator, the output power $P_{DG}(t)$ is calculated according to the following equations:

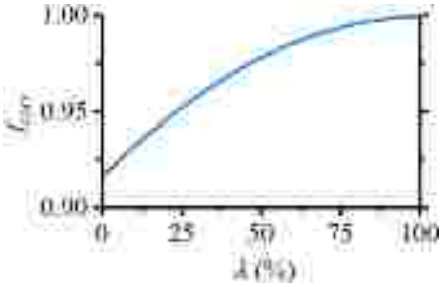

Fig. 2. Efficiency correlation of generators [47].

$$P_{DG}(t) = S_G(t)\eta_G(t)P_D(t) \tag{25}$$

in which

$$P_D(t) = T_D(t)\omega_D(t) \tag{26}$$

$$\eta_G(t) = \eta_{G0} f_{corr}(\lambda(t)) \quad \text{and} \tag{27}$$

$$\lambda(t) = \frac{P_D(t)}{P_{D\_rate}} \tag{28}$$

where $S_G(t)$ is a binary number that denotes the on/off state of the generator and $P_D(t)$ and P_{D_rate} are the output power and the rated power, respectively, of the diesel engine. Considering that efficiency varies with the generator power, the efficiency $\eta_G(t)$ is corrected from the base efficiency η_{G0} following the curve $f_{corr}(\lambda)$ (Fig. 2) [47]. The symbol $\lambda(t)$ represents the ratio of the generator power to its rated power.

2.6. ESS

Lithium-ion batteries are used in the ESS because of high energy density and good storage efficiency [48]. The ESS consists of battery modules that are connected in series. Each module has 40 battery cells. Rint model [15,49] is adopted to model the ESS. For each battery cell, the output current $I_{bat}(t)$ is obtained by [33,50]:

$$I_{bat}(t) = \frac{V_{bat}(t) - \sqrt{{V_{bat}}^2(t) - 4R_{bat}\cdot P_{bat}(t)}}{2R_{bat}} \tag{29}$$

where $V_{bat}(t)$, R_{bat}, and $P_{bat}(t)$ are the open-circuit voltage, internal resistance, and terminal power of the battery cell, respectively.

The dynamics of the battery SOC is expressed as [15]:

$$\dot{SOC}(t) = -\frac{I_{bat}(t)\eta_{colm}}{Q_{bat}} \tag{30}$$

where η_{colm} is the Coulombic efficiency and Q_{bat} is the capacity of the battery.

The overall output power $P_{ESS}(t)$ of the ESS is calculated as:

$$P_{ESS}(t) = 40 n_{ESS} P_{bat}(t) \tag{31}$$

where n_{ESS} is the number of battery modules in the ESS.

3. Problem formulation

The bi-level optimization proposed in this paper integrates component sizing and energy management into a single algorithm. The mathematical description of the optimization problem is given below.

$$\min_{\mathbf{x}}\{f_1(\mathbf{x}), f_2(\mathbf{x}), f_3(\mathbf{x})\}$$
$$s.t.\ \ h_i(\mathbf{x}) = 0,\ \ i = 1, 2, 3, \ldots, m$$
$$g_j(\mathbf{x}) \geqslant 0,\ \ j = 1, 2, 3, \ldots, n, \tag{32}$$

where optimization parameter set $\mathbf{x}$, the optimization objectives ($f_1(\mathbf{x})$, $f_2(\mathbf{x})$, and $f_3(\mathbf{x})$) and constraints ($h_i(\mathbf{x})$ and$g_j(\mathbf{x})$) are defined in the

following subsections:

3.1. Optimization parameters

The optimization parameter set $\mathbf{x}$ consists of nine parameters.

$$\begin{aligned}\mathbf{x} &= (\mathbf{x_S}, \mathbf{x_E}(t))^{\mathrm{T}}\\ \mathbf{x_S} &= (V_D, d_M, l_M, i, n_{ESS})^{\mathrm{T}}\\ \mathbf{x_E}(t) &= (S_{G1}(t), S_{G2}(t), P_{D1}(t), P_{D2}(t))^{\mathrm{T}},\end{aligned} \tag{33}$$

where $\mathbf{x_S}$ is the subset of sizing parameters and $\mathbf{x}_{\mathrm{E}}(t)$ is the subset of energy management parameters. Five elements are included in $\mathbf{x_S}$: the engine cylinder displacement V_D, the motor diameter d_M, the motor lengthl_M, the number of battery modules n_{ESS}, and the gear ratio i. Four time-dependent elements are included in $\mathbf{x}_{\mathrm{E}}(t)$: the binary switch parameters ($S_{G1}(t)$ and$S_{G2}(t)$) and the output power ($P_{D1}(t)$ and $P_{D2}(t)$) of the two DGs.

3.2. Objectives

The following three factors are considered in bi-level optimization: fuel consumption, GHG emission, and NPC. The aforementioned factors are minimized by the upper-level optimization, which calls for the results of the lower-level optimization in each iteration. The lower level is required only to minimize the fuel consumption because the amount of fuel consumption on a voyage determines the GHG emission and the operation cost away from the shore power station.

3.2.1. Fuel consumption ($f_1(\mathbf{x})$)

The total fuel consumption m_{fuel} accounts for the operation and startup of the DGs.

$$f_1(\mathbf{x}) = m_{fuel} = \int_0^{t_{count}} \dot{m}_f(t)\mathrm{d}t + m_{su}n_{su}|_0^{t_{count}} \tag{34}$$

where t_{count} is the time duration considered in the calculation of fuel consumption, m_{su} is the fuel consumption of DG per startup, and n_{su} is the number of the DG startup times during t_{count}. The value of m_{su} is approximately 20% of the fuel consumption at the operating point where the diesel engine offers its maximum power [6].

3.2.2. GHG emission ($f_2(\mathbf{x})$)

The total GHG emission m_{GHG} considers the combustion of the diesel fuel and the generation of the shore electricity.

$$f_2(\mathbf{x}) = m_{GHG} = m_{fuel}I_{fuel} + E_{sho}|_0^{t_{count}} I_{ele} \tag{35}$$

where I_{fuel} is the life cycle average GHG intensity of diesel fuel, E_{sho} is the shore electricity consumed during t_{count}, and I_{ele} is the life cycle average GHG intensity of shore electricity.

3.2.3. NPC ($f_3(\mathbf{x})$)

The *NPC* is used to evaluate the economic feasibility that includes equipment purchase, system operation, and battery replacement [51].

$$f_3(\mathbf{x}) = NPC = N_{ini} + N_{ope} + N_{ESS} \tag{36}$$

whereN_{ini}, N_{ope}, and N_{ESS} are the costs of initial equipment investment, system operation, and battery replacement, respectively.

The initial investment N_{ini} can be expressed as [45]:

$$N_{ini} = 2c_{DG}P_{DG\_rate}(1 + \Delta c_{gen}) + 2c_M P_M \tag{37}$$

where c_{gen} is the unit power cost of the DGs, c_M is the unit power cost of motors, P_{DG_rate} is the rated power of the DGs, P_{M_rate} is the rated power of motors, and Δc_{gen} is the correction factor accounting for electrical components.

The cost of system operation N_{ope} can be obtained by [52]:

$$N_{ope} = \sum_{i=1}^{Y} c_{fuel}m_{fuel}\left(\frac{1+g_{fuel}}{1+I}\right)^i + \sum_{i=1}^{Y} c_{sho}E_{sho}\left(\frac{1+g_{sho}}{1+I}\right)^i \tag{38}$$

where c_{fuel} and c_{sho} are the unit costs of diesel fuel and shore electricity, respectively, g_{fuel} and g_{sho} are the annual inflation rates of diesel fuel and shore electricity, respectively, and I is the annual interest rate.

The cost of battery replacement N_{ESS} can be calculated by [52]:

$$N_{ESS} = \sum_{i=1}^{n_{rep}+1} c_{bat}Q_{ESS}\left(\frac{1+g_{bat}}{1+I}\right)^{iY_{ESS}} \quad \text{and} \tag{39}$$

$$n_{rep} = \begin{cases} \frac{Y}{Y_{ESS}} - 1 & \frac{Y}{Y_{ESS}} - \left[\frac{Y}{Y_{ESS}}\right] = 0 \\ \frac{Y}{Y_{ESS}} & \frac{Y}{Y_{ESS}} - \left[\frac{Y}{Y_{ESS}}\right] \neq 0 \end{cases} \tag{40}$$

where n_{rep} is the total number of battery replacements during service life Y, c_{bat} is the unit cost per capacity of the ESS, Q_{ESS} is the ESS capacity, g_{bat} is the annual inflation rate of the acquisition cost of the battery, and Y_{ESS} is the longevity of lithium-ion battery.

3.3. Constraints

Constraints related to voyage requirements and component capacity limitations are considered for the minimization of the objective functions defined in (32). All the five constraints work for the upper-level optimization, and four of the five (except the constraint of shore power) work for the lower-level optimization. They are detailed in the following subsections.

3.3.1. Power balance constraint

The total power requirement $P_{req}(t)$ accounts for the propulsive load $P_{pro}(t)$ and the auxiliary load $P_{aux}(t)$. The propulsive load $P_{pro}(t)$ is the sum of the input power to the two motors. The auxiliary load $P_{aux}(t)$ includes hotel load $P_{hot}(t)$ and service load $P_{ser}(t)$. The mathematical description is given below.

$$P_{req}(t) = P_{pro}(t) + P_{aux}(t) \tag{41}$$

$$P_{pro}(t) = 2P_{M\_in}(t) \quad \text{and} \tag{42}$$

$$P_{aux}(t) = P_{hot}(t) + P_{ser}(t) \tag{43}$$

The power requirement $P_{req}(t)$ is fulfilled together by the two DGs and the ESS. The mathematical description is given below. By comparing (41) and (44), we can see that there exists a power balance between the power consumers and producers.

$$P_{DG1}(t) + P_{DG2}(t) + P_{ESS}(t) = P_{req}(t) \tag{44}$$

3.3.2. Response time of the DGs

The response time during the startup of the DGs is considered. Therefore, the time interval $(t_{k+1} - t_k)$ between the two startup operations should be greater than the limit t_{DG} [53]. In other words, the DGs cannot start or stop arbitrarily without considering the response time limit.

$$t_{k+1} - t_k \geqslant t_{DG} \tag{45}$$

3.3.3. ESS operation constraint

The ESS is subject to two limits. The first is the *SOC* boundary defined by SOC_{b_low} and SOC_{b_up}. The second is the limitation of the charging and discharging currents defined by $I_{bat\_\min}$ and $I_{bat\_\max}$. The battery current I_{bat} should be within the range.

$$SOC_{b\_low} < SOC(t) < SOC_{b\_up} \tag{46}$$

$$I_{bat\_\min} \leqslant I_{bat}(t) \leqslant I_{bat\_\max} \tag{47}$$

3.3.4. Shore power constraint

The charging time t_{chg} of each voyage should be less than the maximum charging time $t_{chg\_\max}$ scheduled by the voyage. Therefore,

$$t_{chg} \leqslant t_{chg\_max} \tag{48}$$

3.3.5. Maximum speed constraint

The maximum speed v_{max} of the ship should exceed the speed requirement v_{req} of the studied voyage.

$$v_{max} \geqslant v_{req} \tag{49}$$

4. Bi-level optimization method

The flowchart of the proposed bi-level optimization method is depicted in Fig. 3. MOPSO is used for the optimization of the five sizing parameters defined by $\mathbf{x}_S$ at the upper level. An MAECMS is developed for the optimization of the four energy management parameters defined by $\mathbf{x}_E(t)$ at the lower level. The lower level is used to analyze the optimal energy management schedule. The MOPSO algorithm provides feasible sizing parameters to the MAECMS, and the MAECMS provides feedback of the optimal energy management parameters to MOPSO. Afterward, MOPSO evaluates the performance regarding the three optimization objectives and obtain optimal solutions after several iterations.

4.1. MOPSO algorithm

MOPSO is a *meta*-heuristic method inspired by the collective behavior of birds and is widely used to solve constrained nonlinear multi-objective optimization problem because of simplicity, convergence speed, and robustness [54]. Referring to [22], an external repository is adopted by the MOPSO algorithm to archive previously found non-dominated vectors, and the mutation operator acts both on the particles of the swarm and on the range of each design variable of the studied problem. The behavior of a particle j is defined by two attributes: a position vector $\mathbf{x}_{Sj}$ containing the five sizing parameters and a velocity vector $\mathbf{v}_{Sj}$ representing the moving velocity from position $\mathbf{x}_{Sj}$ of the k-th iteration to a specified position of the $(k+1)$-th iteration. The MOPSO algorithm is given below.

1. Initialization

(1) Generate a swarm of original particles randomly for the upper level.

(2) Send the values of the original particles to the lower level, which implements energy management optimization for each particle. Thereafter, in addition to the performance, the values of the five sizing parameters and the four energy management parameters of each particle are stored in its memory.

(3) Initialize the velocities $\mathbf{v}_{Sj}^{k} = 0$ for k = 1, and initialize the

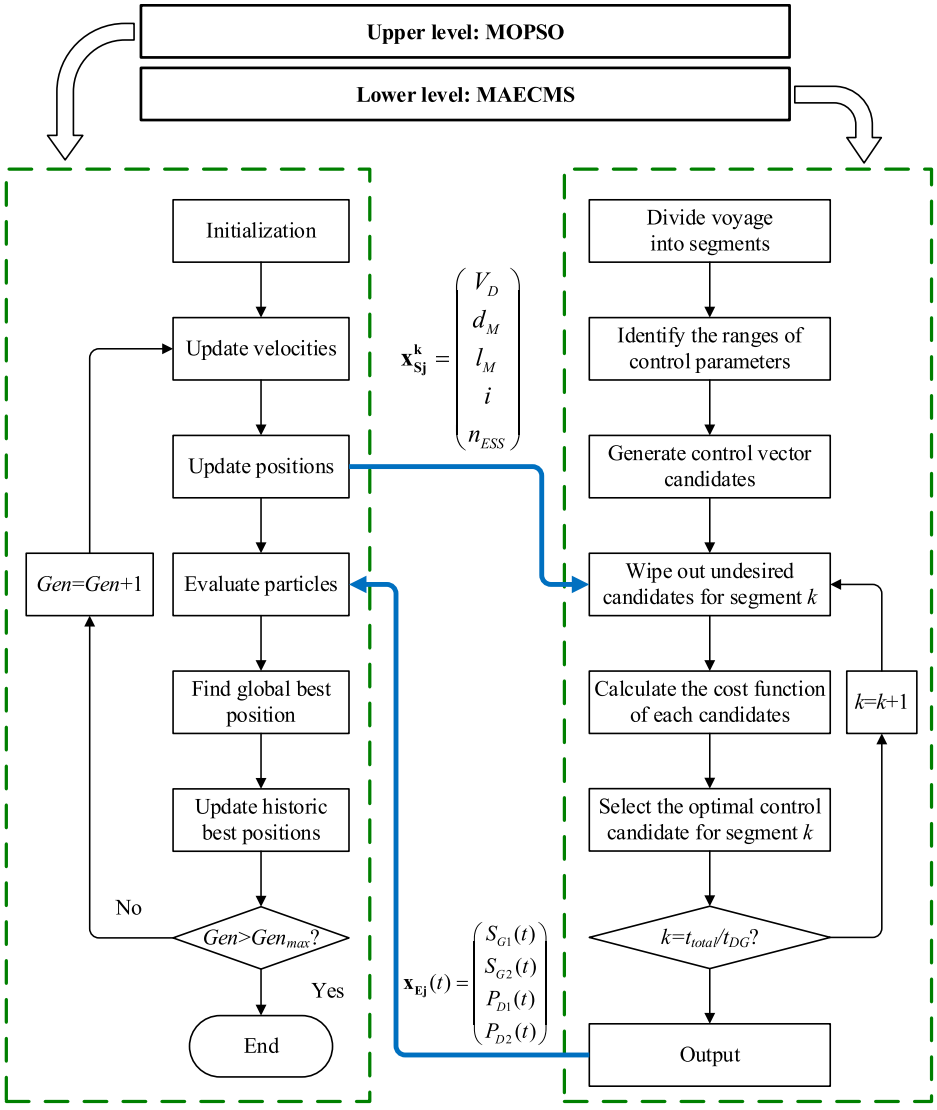

Fig. 3. Flowchart of the proposed bi-level optimization (MOPSO for the upper level and MAECMS for the lower level).

historic best position that particle j has had, $\mathbf{p}^{\mathbf{k}}_{\mathbf{Sj\_best}} = \mathbf{x}_{\mathbf{Sj}}$ for k = 1. Store the non-dominated positions of the original particles in the repository.

(4) Generate hypercubes of the design space explored so far, and locate the particles in the repository in the hypercubes according to the value of objectives.

2. Update the velocities using the following iteration formula:

$$\mathbf{v}^{\mathbf{k+1}}_{\mathbf{Sj}} = \omega \mathbf{v}^{\mathbf{k}}_{\mathbf{Sj}} + a_1 r_1 (\mathbf{p}^{\mathbf{k}}_{\mathbf{Sj\_best}} - \mathbf{x}^{\mathbf{k}}_{\mathbf{Sj}}) + a_2 r_2 (\mathbf{g}^{\mathbf{k}}_{\mathbf{S\_best}} - \mathbf{x}^{\mathbf{k}}_{\mathbf{Sj}}) \tag{50}$$

where $\mathbf{v}^{\mathbf{k+1}}_{\mathbf{Sj}}$ is the velocity of the particle j of the (k + 1) iteration, ω is the inertia weight, a_1 is the cognitive parameter, a_2 is the social parameter, r_1 and r_2 are two random numbers in the range [0,1], $\mathbf{p}^{\mathbf{k}}_{\mathbf{Sj\_best}}$ is the historic best position that particle j has had of the k iteration, and $\mathbf{g}^{\mathbf{k}}_{\mathbf{S\_best}}$ is the position taken from the repository according to the Pareto dominance criterion, which is as follows: Assign the non-empty hypercubes with a fitness index equal to the result of dividing 1 by the number of particles that they contain [22]. Select one hypercube using the roulette wheel selection based on the fitness index. Then, $\mathbf{g}^{\mathbf{k}}_{\mathbf{S\_best}}$ is set to be a particle randomly chosen from the selected hypercube.

3 Update the position of each particle as per the following formula and send them to the lower level:

$$\mathbf{x}^{\mathbf{k+1}}_{\mathbf{Sj}} = \mathbf{x}^{\mathbf{k}}_{\mathbf{Sj}} + \mathbf{v}^{\mathbf{k+1}}_{\mathbf{Sj}} \tag{51}$$

where $\mathbf{x}^{\mathbf{k+1}}_{\mathbf{Sj}}$ is the position of the particle j of the (k + 1) iteration.

4. Send the values of the position of the particles to the lower level and implement energy management optimization. Thereafter, the memory of the particles is stored.

5. Find the global best position $\mathbf{g}^{\mathbf{k+1}}_{\mathbf{S\_best}}$ according to the Pareto dominance criterion as described in step 2.

6. If $\mathbf{p}^{\mathbf{k}}_{\mathbf{Sj\_best}}$ is dominated by the current position $\mathbf{x}^{\mathbf{k}}_{\mathbf{Sj}}$, update the historic best position as $\mathbf{p}^{\mathbf{k+1}}_{\mathbf{Sj\_best}} = \mathbf{x}^{\mathbf{k}}_{\mathbf{Sj}}$. If $\mathbf{p}^{\mathbf{k}}_{\mathbf{Sj\_best}}$ does not dominate or be dominated by $\mathbf{x}^{\mathbf{k}}_{\mathbf{Sj}}$, $\mathbf{p}^{\mathbf{k+1}}_{\mathbf{Sj\_best}}$ is set to be one of the positions $\mathbf{x}^{\mathbf{k}}_{\mathbf{Sj}}$ and $\mathbf{p}^{\mathbf{k}}_{\mathbf{Sj\_best}}$ randomly.

7. Repeat steps 2–5 until the maximum number of iterations $Gen_{\max}$ is achieved.

4.2. MAECMS

This study modifies the traditional adaptive ECMS based on two aspects. The first aspect is to extend the optimization time step, which helps reduce the computational load. As it takes time to realize the values of the four energy management parameters, the optimization time step does not make sense if the step is less than the engine startup time. Generally, diesel engines in mainstream ships take more than 45 s to startup [53]. Moreover, ship voyages are not as changeable as those of cars in urban traffic. Therefore, this study sets the time step, represented by t_{DG}, at 60 s. This measure can reduce the computing time. In addition, to enhance the computational efficiency, the proposed MAECMS eliminates the undesired control candidates before each optimization time step if (52) is satisfied.

$$\begin{cases} P_{DG1}(t) + P_{DG2}(t) - P_{req}(t) < 0, & SOC(t) < SOC_{b\_low} \\ P_{DG1}(t) + P_{DG2}(t) - P_{req}(t) > 0, & SOC(t) > SOC_{b\_up} \end{cases} \tag{52}$$

The second aspect is the calculation of the equivalent factor comparing electrical energy consumption with fuel consumption by considering the current operation of the diesel engines other than the battery SOC. The mathematical derivations are detailed in the following paragraphs:

Basically, the MAECMS assumes that the battery SOC variation at any time will be compensated in the future by the diesel engines [55]. Thus, the equivalent fuel consumption rate $\dot{m}_{f,eqv}(t)$ accounts for two parts: the mass flow of the diesel fuel $\dot{m}_f(t)$ and the virtual fuel consumption rate $\dot{m}_{vir}(t)$.

$$\dot{m}_{f,eqv}(t) = \dot{m}_f(t) + \dot{m}_{vir}(t) \tag{53}$$

The calculation of the virtual fuel consumption rate $\dot{m}_{vir}(t)$ is given by:

$$\dot{m}_{vir}(t) = \frac{s(t)}{H_{LHV}} P_{ESS}(t) \tag{54}$$

where $s(t)$ is the equivalence factor that converts electrical energy consumption into virtual fuel consumption.

The optimization for energy management is resolved by time steps one by one in sequence. In each time step, the control problems are formulated as below:

$$\min_{\mathbf{x_E}(k)} [m_f(k) + m_{vir}(k)],\ k = 1, 2, ..., \frac{t_{total}}{t_{DG}} \tag{55}$$

where

$$m_f(k) = \int_{(k-1)t_{DG}}^{kt_{DG}} \dot{m}_f(t)\mathrm{d}t, \text{ and (56)}$$

$$m_{vir}(k) = \int_{(k-1)t_{DG}}^{kt_{DG}} \dot{m}_{vir}(t)\mathrm{d}t \tag{57}$$

The average efficiency $\bar{\eta}_{\mathrm{DGs}}(k)$ of the two DGs is calculated by:

$$\bar{\eta}_{\mathrm{DGs}}(k) = \frac{\int_{(k-1)t_{DG}}^{k \cdot t_{DG}} (P_{DG1}(t) + P_{DG2}(t))\mathrm{d}t}{H_{LHV} m_f(k)} \tag{58}$$

The electrical energy variation of the ESS is calculated by:

$$\Delta E_{ESS}(k) = \int_{(k-1)t_{DG}}^{k \cdot t_{DG}} (P_{ESS}(t) + P_{ESS\_R}(t))\mathrm{d}t \tag{59}$$

where P_{ESS_R} is the power loss related to the internal resistance of the battery.

Thus, based on the efficiency of the DG operating in the current time step, the virtual fuel consumption $m_{vir}(k)$ can be formulated as below:

$$m_{vir}(k) = \frac{\Delta E_{ESS}(k)}{H_{LHV} \cdot \bar{\eta}_{\mathrm{DGs}}} \tag{60}$$

Substituting (57) and (60) into (54), the equivalence factor $s(k)$ is given by:

$$s(k) = \frac{\Delta E_{ESS}(k)}{\bar{\eta}_{\mathrm{DGs}} \cdot \int_{(k-1)t_{DG}}^{k \cdot t_{DG}} P_{ESS}(t)\mathrm{d}t} \tag{61}$$

Furthermore, substituting (58) and (59) into (61) yields the calculation of $s(k)$ as below:

Table 1
Algorithms and results of three optimization frameworks.

Optimization framework	Algorithm for the upper level	Algorithm for the lower level	Average statistics of the Pareto solution set		
			Fuel consumption (kg)	GHG emission (kg)	NPC (dollar)
Bi-level	MOPSO	MAECMS	5.16×10^5	2.11×10^6	7.70×10^6
Single-upper-level	MOPSO	Heuristic rule	5.55×10^6	2.22×10^6	8.36×10^6
Single-lower-level	Result from the single-upper-level optimization	MAECMS	5.17×10^5	2.14×10^6	8.05×10^6

$$s(k) = \frac{\int_{(k-1)t_{DG}}^{k\cdot t_{DG}} (P_{ESS}(t) + P_{ESS\_R}(t))\mathrm{d}t \cdot \int_{(k-1)t_{DG}}^{k\cdot t_{DG}} \dot{m}_f(t) H_{LHV}\,\mathrm{d}t}{\int_{(k-1)t_{DG}}^{k\cdot t_{DG}} (P_{DG1}(t) + P_{DG2}(t))\mathrm{d}t \cdot \int_{(k-1)t_{DG}}^{k\cdot t_{DG}} P_{ESS}(t)\mathrm{d}t} \quad (62)$$

By using (62), the MAECMS has been developed for instantaneous optimization depending on the system variables at the current time based on Pontryagin's minimum principle [33]. The flowchart is depicted in Fig. 3. Afterward, the values of the four energy management parameters are sent back to the upper level.

A comparison among the proposed MAECMS, DP, and AECMS is provided in Table A.1. These are implemented for the optimization of the energy management strategy for the same HEPS whose sizes are selected from the bi-level optimal solution set in Table 2. The results show that the fuel consumption of MAECMS is only 2.44% more than that of the DP; however, the computing time of MAECMES is one-187 of the DP. In other words, the MAECMS is much more efficient with fuel consumption. In addition, compared with the AECMS [35], the proposed MAECMS decreases fuel consumption by 1.37% and reduces computing time by 62.27%. The operating schedules of the diesel generators under the three energy management strategies are illustrated in Fig. A1. Therefore, the MAECMS is the most suitable strategy for complex bi-level optimization.

5. Results and discussion

In this section, the operating cycle of a tug ship is defined considering propulsive load, operational load, and hotel load. Next, the Pareto solution set obtained by the proposed bi-level optimization is illustrated and compared with single-upper-level and single-lower-level optimizations. Thereafter, three optimal solutions are selected from the Pareto solution sets according to the technique for order preference by similarity to ideal solution (TOPSIS) [56,57], the simulation results of the three optimal designs under the operating cycle are compared and analyzed.

5.1. Operating cycle

In the absence of a standardized operation cycle for AHTS vessels, a speed profile of a tug ship collected from real operation data is adopted in this study [58] (Fig. 4). There are two modes of speed profile: sea mode and maneuvering mode. In the sea mode, the AHTS vessel sails at a speed of ~ 5.14 m/s to arrive at operation sites. In the maneuvering mode, the vessel sails at a low speed and performs operations such as lifting and pulling. Thus, the propulsive load can be calculated from the speed profile. The auxiliary load (non-propulsive load), comprising operational load and hotel load, cannot be ignored for the AHTS vessel. Considering the power demand of cranes and capstans, the operational load and hotel load are estimated in Fig. 4. Before each voyage, the battery is charged to the upper limit at the shore power plant. The duration of the profile plotted in Fig. 4 is 4800 s. The AHTS is supposed to run 6 times a day and 200 days per year.

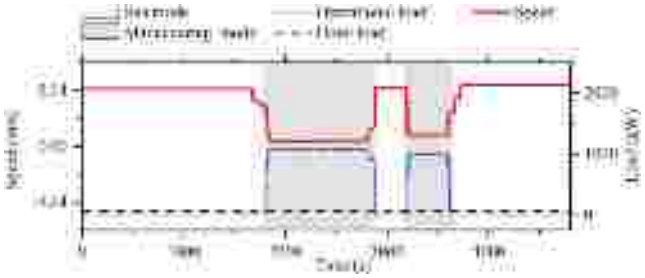

Fig. 4. Operating profile of the studied AHTS vessel, including speed profile, operational load, and hotel load [58].

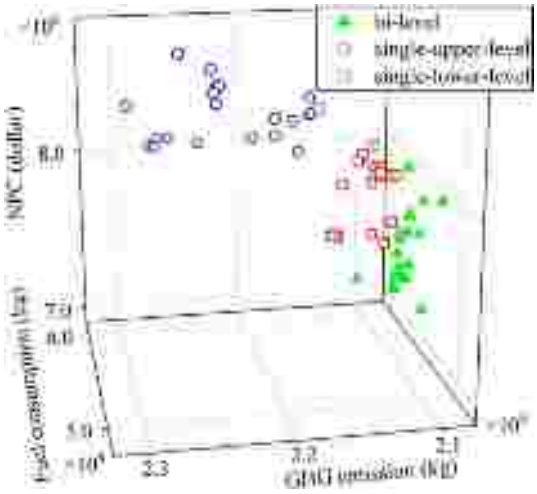

Fig. 5. Pareto solution sets.

5.2. Pareto solution sets

The parameters used for optimization are given in Table A.2. The ranges of the optimization variables are given in Table 2. The Pareto solution set obtained from the proposed bi-level optimization is plotted in a three-dimensional coordinate system representing annual fuel consumption, annual GHG emission, and lifecycle NPC (Fig. 5). For convenient observation, the Pareto front is projected as two-dimensional coordinates as shown in Fig. 6.

In addition, two types of conventional single-level optimization are carried out for comparisons. As listed in Table 1, the single-upper-level optimization adopts the same MOPSO algorithm as the bi-level optimization for component sizing at the upper level but uses a heuristic rule-based energy management strategy for the lower level, which has been widely applied in the field of hybrid electric propulsion design [59,60]. On the other hand, the single-lower-level optimization adopts the MAECMS, which is also adopted by the bi-level optimization, however, based on a fixed set of component sizes. In this study, the single-lower-level optimization inherits optimal solutions obtained from the single-upper-level optimization. With regard to the single-level optimization, the successive implementation of the single-upper-level and single-lower-level optimizations is believed to yield the best result.

Table 2
Range of the optimization variables and optimal solutions.

Optimization variable	Range	Bi-level ($\mathbf{X_b}$)	Single-level ($\mathbf{X_{s\_u}}$, $\mathbf{X_{s\_l}}$)
Displacement of the diesel engine V_D (10^{-3} m^3)	[57.00 97.00]	59.95	83.46
Diameter of the motor rotor d_M (m)	[0.31 0.85]	0.59	0.48
Length of the motor rotor l_M (m)	[0.25 0.95]	0.25	0.69
Gear ratio i	[820]	19.48	15.48
Number of the battery module in series n_{ESS}	[40200]	131	200

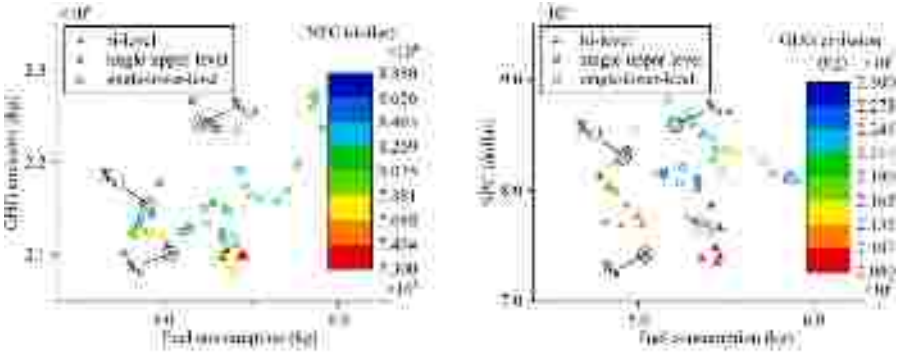

(a) Projection on fuel consumption–GHG emission plane (b) Projection on fuel consumption–NPC plane

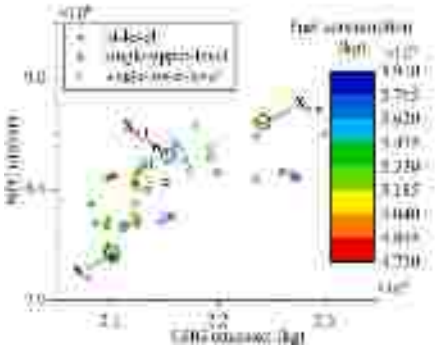

(c) Projection on GHG emission–NPC plane

Fig. 6. Projection of Pareto front on two-dimensional planes (circles: solutions selected by the TOPSIS).

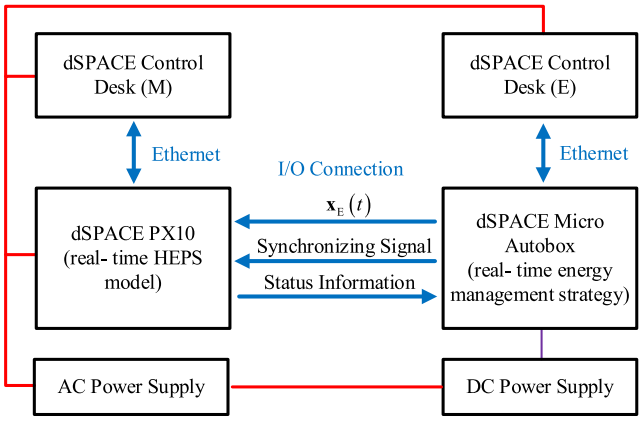

Fig. 7. Schematic diagram of the HIL experimental platform.

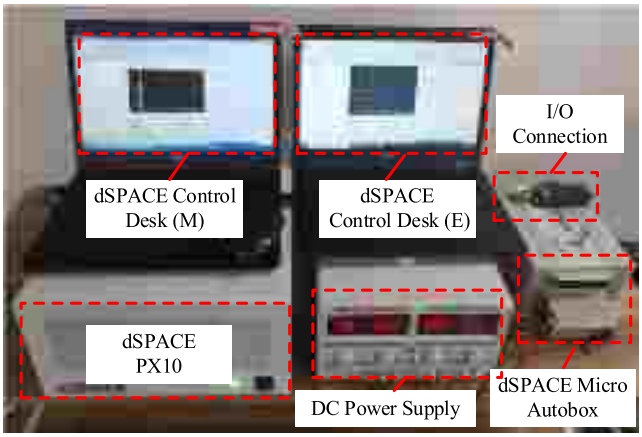

Fig. 8. Photo of the HIL experimental platform.

Three Pareto solution sets are illustrated in Fig. 5, representing the optimal results from the bi-level (triangles), single-upper-level (circles), and single-lower-level (squares) optimizations, respectively. Overall, regarding the GHG emission and NPC, the triangles are closer to the smaller part of the coordinate axis, the squares are relatively away from the smaller part, and the circles are the farthest. The three sets are not that distinguishable in terms of fuel consumption.

Projection regarding the two-dimensional coordinates shows the detailed differences in Fig. 6. The three Pareto solution sets are also represented by triangles, circles, and squares. In each two-dimensional coordinate, the color, defined by the color scale, represents the value of the solution on the third coordinate axis. The projection on the fuel consumption–GHG emission plane in Fig. 6(a) states that the fuel consumption of the bi-level optimization is roughly the same as that of the single-lower-level optimization and is obviously less than that of the single-upper-level optimization. The same conclusion is drawn from Fig. 6(b).

The average statistics of the three Pareto solution sets are provided in Table 1. The average fuel consumption of the bi-level optimization is 0.2% less than that of the single-lower-level optimization and 7.03% less than that of the single-upper-level optimization; the average GHG emission of the bi-level optimization is 1.40% less than that of the single-lower-level optimization and 3.60% less than that of the single-upper-level optimization; the average NPC of the bi-level optimization is 4.35% less than that of the single-lower-level optimization and 7.89% less than that of the single-upper-level optimization. Overall, the best results are obtained by the bi-level optimization, followed by the single-lower-level and single-upper-level optimizations. The optimal match of the component sizing and energy management contributes to the high performance of the bi-level optimization. The insights are given in the next section.

As previously described, the single-lower-level optimization inherits optimal component sizes obtained from the single-upper-level optimization. Hence, the energy management policy, i.e., MAECMS, contributes to the improvement of the single-lower-level optimization

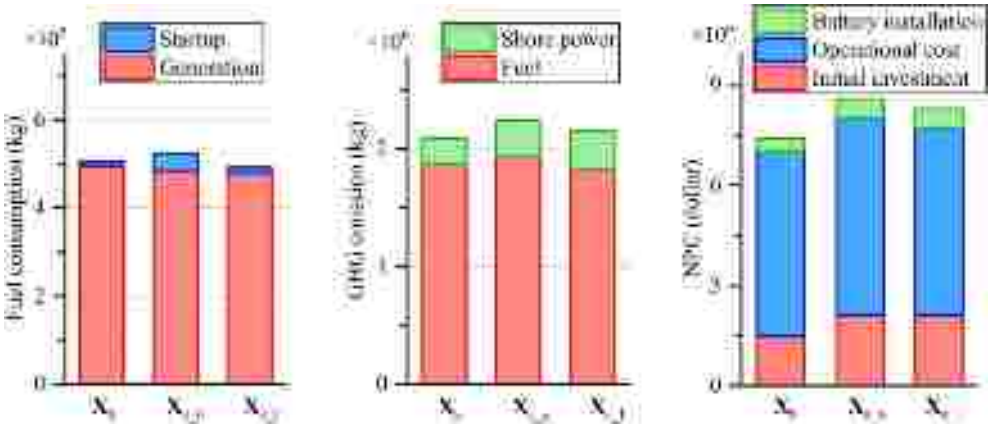

(a) Annual fuel consumption (b) Annual GHG mission (c) Lifecycle NPC

Fig. 9. Composition of evaluation indicators of the three selected solutions.

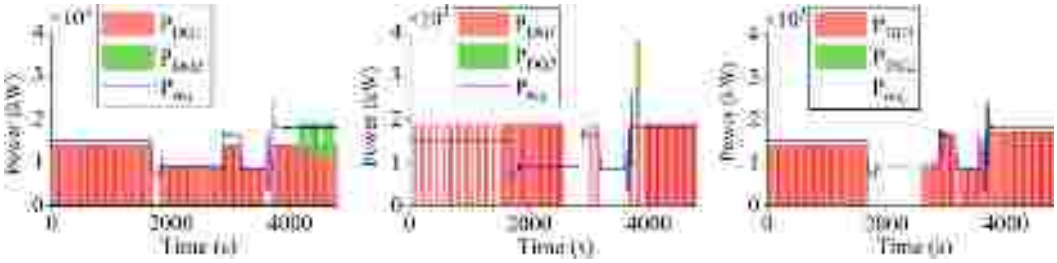

(a) $\mathbf{X}_b$ (b) $\mathbf{X}_{s\_u}$ (c) $\mathbf{X}_{s\_l}$

Fig. 10. Operating schedule of the diesel generators of the three selected solutions.

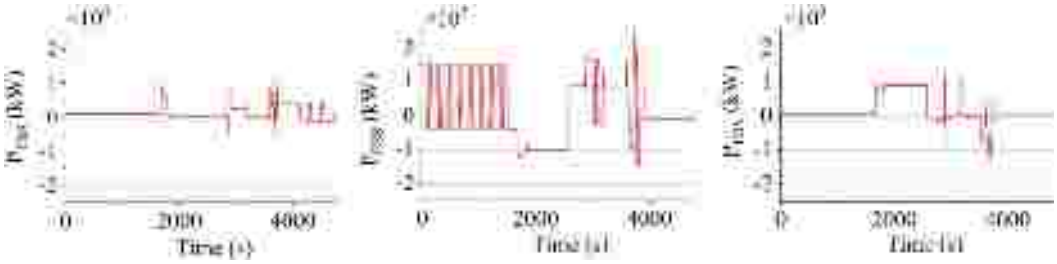

(a) $\mathbf{X}_b$ (b) $\mathbf{X}_{s\_u}$ (c) $\mathbf{X}_{s\_l}$

Fig. 11. Comparison of the battery power of the three selected solutions.

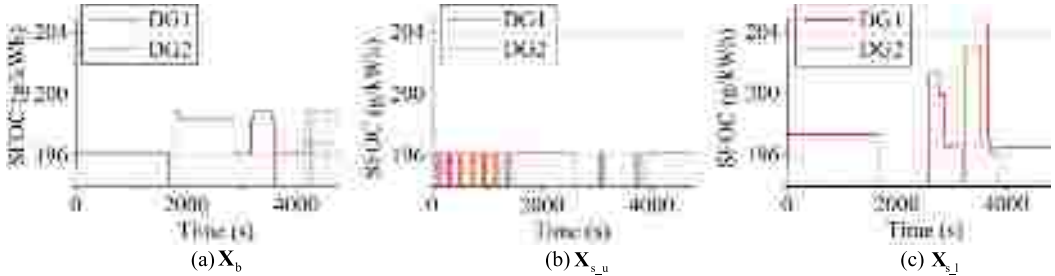

(a) $\mathbf{X}_b$ (b) $\mathbf{X}_{s\_u}$ (c) $\mathbf{X}_{s\_l}$

Fig. 12. Comparison of the SFOC of the diesel generators of the three selected solutions.

rather than the single-upper-level optimization. The MAECMS considers fuel consumption by the engines and electricity consumption from the batteries. The fuel consumed at the engine startup is included in the total fule consumption. However, according to the heuristic method adopted by the single-upper-level optimization, the engines operated at their rated power. Usually, the rated power is not exactly equal to the required load power. The gap is filled by charging and discharging of the batteries. When the batteries are charged to their SOC upper limit, the engines have to be stopped. On the other hand, when the batteries are discharged to their SOC lower limit, the engines have to be re-started. Frequent restarts lead to more fuel consumption. The MAECMS has solved this issue by appropriately reducing the engine power and the number of times the engine restarts. The results validate the significance of the advance energy management and also the correctness

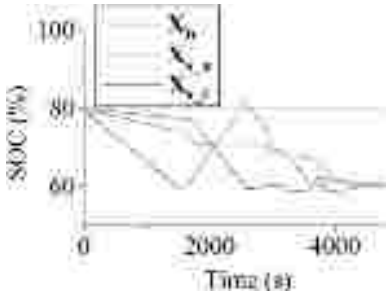

Fig. 13. Comparison of the SOC trajectory of the three selected solutions.

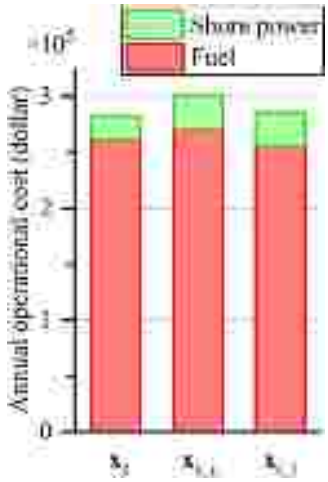

Fig. 14. Comparison of the annual operational cost of the three selected solutions.

of the programs developed for this study.

5.2.1. Selection of optimal solutions from the Pareto sets

Based on the above results, for better understanding, an optimal solution is selected from each Pareto solution set based on the TOPSIS, which is a robust criterion of decision-making for multiple objective problems [56,57]. In the TOPSIS, two virtual points, ideal point and nadir point, are defined. The ideal point reaches the minimum in terms of each of the three performance indexes in the Pareto solution set. On the contrary, the nadir point reaches the maximum. Non-dimensionalization is processed to define the possibility of different dimensions of objectives as given below [56]:

$$s_{ij} = \frac{F_{ij}}{\sqrt{\sum_{i=1}^{o} (F_{ij})^2}} \tag{63}$$

where F is the objective matrix of each point in the Pareto solution set, the subscript i is the number of each point, j is the index for each objective, and o is the total number of the objectives, which equals to three in this study.

The TOPSIS defines the distance D_{i+} from a random point in the Pareto solution set to the ideal point, and the distance D_{i-} from a random point to the nadir point.

$$D_{i+} = \sqrt{\sum_{j=1}^{o} (s_{ij} - s_j^{ideal})^2} \quad \text{and} \tag{64}$$

$$D_{i-} = \sqrt{\sum_{j=1}^{o} (s_{ij} - s_j^{nadir})^2} \tag{65}$$

where s_j^{ideal} is the i^{th} non-dimensional objective of the ideal point calculated by (63); similarly, s_j^{nadir} is the non-dimensional objective of the nadir point.

The larger the value of the variable R_i (defined below), the closer it would be to the ideal point and farther to the nadir point. Therefore, the TOPSIS selects the optimal solution by finding out the maximum R_i [57].

$$R_i = \frac{D_{i-}}{D_{i-} + D_{i+}} \tag{66}$$

The optimal solution selected from the Pareto set regarding the bi-level optimization is represented by $\mathbf{X}_b$, which is denoted by a black circle in Fig. 6. Its component sizes are provided in Table 2. Similarly, the optimal solutions selected from the single-upper-level and single-lower-level optimizations are represented by $\mathbf{X}_{s\_u}$ and $\mathbf{X}_{s\_l}$, which are also denoted by black circles in Fig. 6. Their component sizes are the same, which are provided in Table 2.

5.3. Results under the operating cycle

5.3.1. HIL experiment

To evaluate the performance of the three solutions, HIL experiments are conducted under the operating cycle. The performance evaluation indicators and their compositions are compared with the data collected from the experiments.

The development steps of the HIL experimental platform are as follows: First, the HEPS model and the energy management model built in the MATLAB/Simulink environment are transformed into C code. Second, the C code is downloaded into the dSPACE PX10 platform using dSPACE Control Desk (denoted by M) through the Ethernet. Third, dSPACE Control Desk (denoted by E) downloads the C code of the energy management strategy into dSPACE MicroAutobox. As shown in Fig. 7, dSPACE MicroAutobox is supported by a direct current (DC) power supply, while other objectives of the HIL experimental platform are supported by an alternating current (AC) power supply. The dSPACE MicroAutobox platform sends the energy management parameters $\mathbf{x}_E(t)$ and synchronizing signals to the dSPACE PX10 platform through I/O connection. At the same time, the dSPACE PX10 platform fed the status information of the HEPS back to the dSPACE MicroAutobox platform. Fig. 8 shows the HIL experimental platform.

5.3.2. Performance comparison of the selected solutions

As seen in Table 2, both the component sizes of the bi-level and single-level optimal solutions are within the range of the optimization variables. The most obvious difference between them lies in the size of the engines and number of batteries. The bi-level optimization yields the solution, which benefits from the synchronous optimization of the energy management strategy, with smaller engines and fewer battery modules. The performance indexes and their compositions are compared in Fig. 9.

The fuel consumption has two parts. The first part is consumed by the diesel engines to generate electricity. The second part is used to start up the engines. As shown in Fig. 9(a), regarding the first part, $\mathbf{X}_b$ consumes up to 4.96×10^5 kg, compared to $\mathbf{X}_{s\_u}$ (4.85×10^5 kg) and $\mathbf{X}_{s\_l}$ (4.79×10^5 kg). However, regarding the second part, $\mathbf{X}_b$ consumes as little as 8.36×10^3 kg, compared to $\mathbf{X}_{s\_u}$ (3.68×10^4 kg) and $\mathbf{X}_{s\_l}$ (1.26×10^4 kg). Overall, $\mathbf{X}_{s\_l}$ has the minimum fuel consumption (4.92×10^5 kg), followed by $\mathbf{X}_b$ (5.04×10^5 kg) and $\mathbf{X}_{s\_u}$ (5.22×10^5 kg). $\mathbf{X}_{s\_l}$ has surpassed $\mathbf{X}_b$ because $\mathbf{X}_{s\_l}$ can utilize more electricity from the shore power because of its large battery capacity. The disadvantages of large battery capacity are increasing GHG mission and high cost, which are explained in the following paragraphs.

The GHG emission is caused by two energy sources. One source is fuel engines. High fuel consumption leads to more GHG emissions. Therefore, as shown in Fig. 9(b), the bottom part of $\mathbf{X}_{s\_u}$ is more than that of the other two, which is corresponding to the trend of fuel consumption. The other emission source is the electricity supplied by the shore power plant. $\mathbf{X}_b$ uses less electricity than the two single-level optimal solutions, $\mathbf{X}_{s\_u}$ and $\mathbf{X}_{s\_l}$. Therefore, $\mathbf{X}_b$ emits less GHG (2.21×10^5 kg) from electricity; by contrast, $\mathbf{X}_{s\_u}$ emits 3.06×10^5 kg, and $\mathbf{X}_{s\_l}$ emits 3.28×10^5 kg. By summing up the amount of emissions

from the two sources, $\mathbf{X}_b$ emits the minimum (2.09×10^6 kg), followed by $\mathbf{X}_{s\_l}$ (2.15×10^6 kg) and $\mathbf{X}_{s\_u}$ (2.24×10^6 kg).

The lifecycle NPC can be classified into three parts. The first part involves the initial investment except the battery modules. $\mathbf{X}_b$ uses small engines; so, it costs less; on the contrary, $\mathbf{X}_{s\_u}$ and $\mathbf{X}_{s\_l}$ use large engines; so, they cost more. The second part is the operational cost, which is related to the consumption of fuel and shore electricity. The operational costs of $\mathbf{X}_b$, $\mathbf{X}_{s\_u}$ and $\mathbf{X}_{s\_l}$ are $\$5.55 \times 10^6$, $\$5.91 \times 10^6$ and $\$5.62 \times 10^6$ respectively. The third part is the cost of battery installation and replacement. $\mathbf{X}_b$ uses fewer battery modules, which cost $\$3.1 \times 10^5$; on the contrary, $\mathbf{X}_{s\_u}$ and $\mathbf{X}_{s\_l}$ use more battery modules which cost $\$5.66 \times 10^5$. To sum up, $\mathbf{X}_b$ costs the least as $\$7.40 \times 10^6$, followed by $\mathbf{X}_{s\_l}$ 8.30×10^6 kg and $\mathbf{X}_{s\_u}$ 8.60×10^6 kg.

Overall, compared with the conventional single-upper-level optimization, the solution $\mathbf{X}_b$ of the bi-level optimization achieves 3.37% less fuel consumption, 6.70% less GHG emission, and 13.95% less NPC. When compared with the solution of the single-lower-level optimization, which is believed to be the best solution, $\mathbf{X}_b$ consumes 2.44% more fuel but 2.79% less GHG emission and 10.84% less NPC. The comparison of these results shows that $\mathbf{X}_b$ has significant advantages regarding GHG emission and NPC because of small engines and few batteries. The variable variations under the operating cycle are illustrated and analyzed in the next section.

5.3.3. Variable variations under the operating cycle

The comparisons of the simulation results of the three optimal solutions under every operating cycle (4800 s) are illustrated in Figs. 10–13. Besides, the compositions of the annual operational cost are shown in Fig. 14. Because of different component sizes and energy management strategies, the results differ in terms of engine working time, number of times the engine restarts, specific fuel oil consumption (SFOC) of the diesel engines, battery power, and battery SOC, which cause the performance to be different among the three solutions. The comparison between $\mathbf{X}_b$ and $\mathbf{X}_{s\_u}$ is narrated below, and then the comparison between $\mathbf{X}_b$ and $\mathbf{X}_{s\_l}$ is stated.

As described, $\mathbf{X}_b$ uses small engines and few battery modules coordinated by the MAECMS, considering the fuel consumption of the engines and equivalent fuel consumption of the electricity as given in. Moreover, the fuel consumption of during normal course and startup is included. As a result, $\mathbf{X}_{s\_u}$ uses big engines and more battery modules coordinated by heuristic rules that, in principle, allow the engines to output the rated power. The two diesel generators of the studied HEPS are represented by DG1 and DG2. Most of the time, the output of the diesel generator power of $\mathbf{X}_b$ is slightly less than the demanded power as shown in Fig. 10(a), and its battery gets gradually discharged to fill the power gap as shown in Fig. 11(a). Benefiting from the MAECMS, the number of engine startup times is as few as 6 (3 for DG1 and 3 for DG2). On the contrary, the DG output power of $\mathbf{X}_{s\_u}$, which equals to the rated power of the big engines, is more than the demanded power. Then, the extra power is utilized to charge the battery. Considering the time (t_{DG}) required to start or shut down the DGs, once the battery current reaches 60.00% of the charging limit I_{bat_min}, the battery should be discharged, and the engines have to be shut down. The engines are restarted when the battery discharging current reaches 60.00% of the discharging limit I_{bat_max}or SOC reaches the lower bound SOC_{b_low}. The number of engine startup times increases to 19 (18 for DG1 and 1 for DG2). Therefore, the fuel consumption of $\mathbf{X}_b$ is much less than that of $\mathbf{X}_{s\_u}$, as shown in Fig. 9(a). On the other hand, the SFOC of $\mathbf{X}_b$(Fig. 12(b)) is basically larger than that of $\mathbf{X}_{s\_u}$ (maintained to be 196.20 g/kWh), which means the engine efficiency of $\mathbf{X}_b$ during operation is higher than that of $\mathbf{X}_{s\_u}$. The cumulative working time of the two engines of $\mathbf{X}_b$ is 5100.00 s, which is more than that of $\mathbf{X}_{s\_u}$ (3000.00 s). Therefore, the fuel consumption of the normal running of $\mathbf{X}_b$ is more than that of $\mathbf{X}_{s\_u}$, which explains the data in Fig. 9(a). Nevertheless, according to Fig. 9(a), the total fuel consumption of $\mathbf{X}_b$ is less than that of $\mathbf{X}_{s\_u}$. In short, $\mathbf{X}_b$ reduces fuel consumption by reducing the number of engine startup times, taking advantage of its energy management strategy.

Regarding the GHG emission, electricity from the shore power plant is ignorable as modelled in. The number of battery modules listed in Table 2 shows that the battery capacity of $\mathbf{X}_b$ is much less than that of $\mathbf{X}_{s\_u}$. Accordingly, the battery power during operation of $\mathbf{X}_b$ is much less than that of $\mathbf{X}_{s\_u}$, as shown in Fig. 11. As the battery is charged to the upper bound SOC_{b_up} before the start of each voyage and is discharged to the lower limit SOC_{b_low} at the end of each voyage, as shown in Fig. 13, the amount of electricity consumed by $\mathbf{X}_b$ is much less than that by $\mathbf{X}_{s\_u}$, so is the GHG emission from the shore power plant. In addition, because of the less fuel usage of $\mathbf{X}_b$, less GHG is emitted by $\mathbf{X}_b$. Therefore, the overall GHG emission of $\mathbf{X}_b$ is less than that of $\mathbf{X}_{s\_u}$, which explains the results in Fig. 9 (b). For the same reason that $\mathbf{X}_b$ consumes less fuel and electricity, the operational cost of $\mathbf{X}_b$, which includes the costs of fuel and electricity from the shore power plant, is less than that of $\mathbf{X}_{s\_u}$, as shown in Fig. 14.

As to $\mathbf{X}_b$ and $\mathbf{X}_{s\_l}$, they are using the same energy management strategy, i.e., MAECMS, but their component sizes are much different. As mentioned, $\mathbf{X}_b$ has small engines and few battery modules, which is in contrast to $\mathbf{X}_{s\_l}$. As shown in Fig. 10(a) and (c), most often, the DG output power of both $\mathbf{X}_b$ and $\mathbf{X}_{s\_l}$ is slightly less than the demanded power. Their engines are not always working in high efficiency area because the engine SFOC is not always low as seen in Fig. 12(a) and (c). However, benefiting from the large battery capacity, a large quantity of electricity can be utilized; so, the minimum working time of $\mathbf{X}_{s\_l}$ is 3900 s, and the minimum number of startup times is 4. Thus, the fuel consumption is a bit less than that of $\mathbf{X}_b$.

Large battery capacity allows for long duration of battery discharging to propel a ship. For example, from 1680 s to 2520 s, the pure electricity propulsion mode of $\mathbf{X}_{s\_l}$ lasts 840 s at the discharging power of $\sim$ 900 kW. However, the longest duration of pure electricity propulsion mode of $\mathbf{X}_b$ is 120 s (from 1680 s to 1800 s), at the average discharging power of 650 kW. Nevertheless, the high consumption of electricity emits more GHG, which cannot be ignored especially when the electricity is produced by coal in China and India [61]. The total GHG emission of $\mathbf{X}_{s\_l}$ is more than that of $\mathbf{X}_b$ in spite of less fuel consumption of $\mathbf{X}_{s\_l}$. Moreover, for the same reason that more electricity is consumed by $\mathbf{X}_{s\_l}$, the total operational cost of $\mathbf{X}_{s\_l}$ is more than that of $\mathbf{X}_b$. In a word, confined by the component sizes that are determined by the single-upper-level optimization, $\mathbf{X}_{s\_l}$ is inferior to $\mathbf{X}_b$ in terms of GHG emission and cost.

To sum up, the bi-level optimization is significantly superior to the two single-level optimizations. Specifically, the optimal solution of the single-lower-level optimization is closer in terms of performance to that of the bi-level optimization than that of the conventional single-upper-level optimization.

6. Conclusion

This paper proposes a multiobjective bi-level optimization, which consists of MOPSO for component sizing at the upper level and MAECMS for energy management at the lower level. The optimization considers the following three objectives: fuel consumption, GHG emission, and lifecycle cost. The optimal solution is selected from the Pareto set. Performance experiments are carried out on a real-time HIL platform. The results indicate that the bi-level optimization finds optimal solution resulting in 3.37% less fuel consumption, 6.70% less GHG emission, and 13.95% less NPC compared to the conventional single-upper-level optimization. Furthermore, when compared with the single-lower-level optimization, which is believed to obtain the best solution in the single-level area because it inherits the component sizes from the single-upper-level optimization and adopts the AECMS for energy management, the bi-level optimization exhibits advantages by emitting 2.79% less GHG and incurring 10.84% less NPC at the expense of 2.44% more fuel consumption compared to the single-level optimization. With respect to environmental protection and cost reduction, the bi-level optimization is of importance for the design of HEPSs especially in areas under strict

environmental control and for cost-sensitive ship owners. The proposed bi-level optimization method can be applied to various HEPSs, such as offshore vessels, research, and exploration vessels.

Declaration of Competing Interest

The authors declared that there is no conflict of interest

Appendix

See Tables A1 and A2 and Fig. A1.

Table A1
Comparison among DP, MAECMS and AECMS.

Lower-level optimization method for energy management strategy	Fuel consumption (kg)	Difference with DP	Computing time (s)
DP	4.92×10^5	N/A	7.48×10^4
MAECMS	5.04×10^5	2.44%	400.00
AECMS	5.11×10^5	2.86%	1060.00

Table A2
Parameters used in the simulation.

Parameter	Value	Reference	Parameter	Value	Reference
A_e/A_o	0.54	[62]	Z	4.00	[62]
$A_T(m^2)$	128.60	[62]	c_{bat} ($/kWh)	175.00	[45]
C_{Air}	0.80		c_{DG} ($/kW)	350.00	[45]
C_F	2.27×10^{-3}		c_{fuel}($/kWh)	520.00	[1]
C_W	2.75×10^{-3}		c_M($/kW)	32.00	[45]
D (m)	4.00	[62]	c_{sho}($/kWh)	0.08	[45]
Gen_{max}	100.00		g_{bat} (\%)	3.00	[52]
H_{LHV} (J/kg)	4.27×10^7	[63]	g_{fuel}(\%)	3.00	[52]
I (\%)	5.00	[52]	g_{sho}(\%)	3.00	[52]
$I_{fuel}(kg/kg)$	3.71	[64]	m(kg)	1.70×10^6	[62]
I_{ele} (kg/kWh)	0.86	[65]	t_1	0.10	[38]
I_{bat_min} (A)	−41.00		t_{DG} (s)	60.00	[53]
I_{bat_max} (A)	82.00		t_{chg_max} (s)	3600.00	
Q_{bat} (Ah)	41.00	[45]	v_{req}\;(m/s)	7.71 (or 15.00 kn)	
S_{hull} (m^2)	1347.12	[62]	Δc_{gen} (\%)	6.00	[1].
SOC_{b_low} (%)	60.00		η_{Gb}	0.98	[68]
SOC_{b_up} (%)	80.00		η_{G0}	0.97	[47]
Y\;(year)	25.00	[66]	ρ (kg/m^3)	1.03×10^3	[38]
Y_{ESS}\;(year)	5.00	[67]			

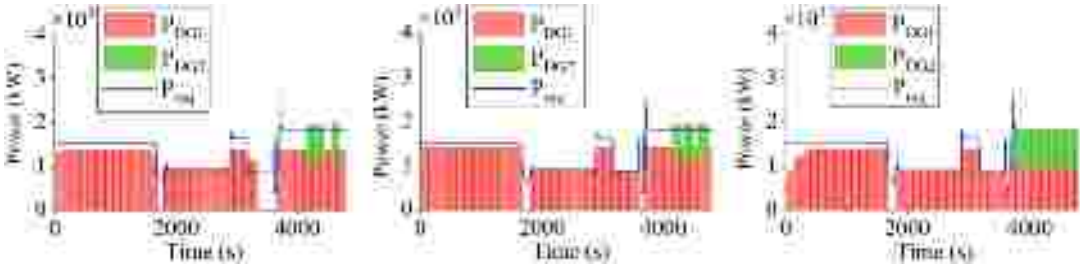

(a) DP (b) MAECMS (c) AECMS

Fig. A1. Operating schedule of the diesel generators under the three energy management strategies.

Acknowledgment

The paper is financially supported by the National Natural Science Foundation of China (No. 51475284), along with the research on the design and construction technology of medium-sized cruise ships, and Key Laboratory of Marine Intelligent Equipment and System of Ministry of Education, Shanghai Jiao Tong University, Shanghai, China.

References

[1] Dedes EK, Hudson DA, Turnock SR. Assessing the potential of hybrid energy technology to reduce exhaust emissions from global shipping. Energ Policy 2012;40:204–18.
[2] Barrett J, Boyd E, Stewart T, Mckenna R, Aspin J, Eldridge J, et al. Hybrid propulsion systems; US2011.
[3] Sciberras EA, Norman RA. Multi-objective design of a hybrid propulsion system for marine vessels. IET Electr Syst Transp 2012;2:148–57.
[4] Hou J, Sun J, Hofmann H. Control development and performance evaluation for battery/flywheel hybrid energy storage solutions to mitigate load fluctuations in all-electric ship propulsion systems. Appl Energy. 2018;212:919–30.
[5] Solem S, Fagerholt K, Erikstad SO, Patricksson Ø. Optimization of diesel electric machinery system configuration in conceptual ship design. J Mar Sci Tech-Japan 2015;20:406–16.
[6] Kanellos FD, Anvari-Moghaddam A, Guerrero JM. A cost-effective and emission-aware power management system for ships with integrated full electric propulsion.

Electr Pow Syst Res 2017;150:63–75.
[7] Pizzo AD, Polito RM, Rizzo R, Tricoli P. Design criteria of on-board propulsion for hybrid electric boats. Xix international conference on electrical machines. 2010. p. 1–6.
[8] Soleymani M, Yoosofi A, Kandi-D M. Sizing and energy management of a medium hybrid electric boat. J Mar Sci Tech-Japan 2015;20:739–51.
[9] Zhu J, Chen L, Wang B, Xia L. Optimal design of a hybrid electric propulsive system for an anchor handling tug supply vessel. Appl Energy 2018;226:423–36.
[10] Dedes EK, Hudson DA, Turnock SR. Investigation of diesel hybrid systems for fuel oil reduction in slow speed ocean going ships. Energy 2016;114:444–56.
[11] Sciberras EA, Zahawi B, Atkinson DJ, Breijs A, van Vugt JH. Managing shipboard energy: a stochastic approach special issue on marine systems electrification. IEEE Trans Transp Electrific 2016;2(4):538–46. https://doi.org/10.1109/TTE.2016.2587682.
[12] Zhang J, Li KJ, Wang M, Lee WJ, Gao H, Zhang C, et al. A bi-level program for the planning of an islanded microgrid including CAES. IEEE Trans Ind Appl 2016;52:2768–77.
[13] Shang C, Srinivasan D, Reindl T. Generation-scheduling-coupled battery sizing of stand-alone hybrid power systems. Energy 2016;114:671–82.
[14] Silvas E, Bergshoeff E, Hofman T, Steinbuch M. Comparison of bi-level optimization frameworks for sizing and control of a hybrid electric vehicle. Vehic Power Propuls Conf 2014.
[15] Xu L, Mueller CD, Li J, Ouyang M, Hu Z. Multi-objective component sizing based on optimal energy management strategy of fuel cell electric vehicles. Appl Energy 2015;157:664–74.
[16] Ghosh S, Ghoshal SP, Ghosh S. Optimal sizing and placement of distributed generation in a network system. Int J Electr Power Energy Syst 2010;32:849–56.
[17] Yang H, Huang C, Wang G, Meng S. Multi-objective optimization of dielectric layer PBG filter structure on the weighting factors method and the response surface methodology. IEEE Mtt-s Int Conf Numer Electromagn Multiphys Model Optim 2016.
[18] Mora AM, Merelo JJ, Castillo PA, Arenas MG. HCHAC: a family of MOACO algorithms for the resolution of the bi-criteria military unit pathfinding problem. Comput Oper Res 2013;40:1524–51.
[19] Ahmadi P, Dincer I, Rosen MA. Multi-objective optimization of a novel solar-based multigeneration energy system. Sol Energy 2014;108:576–91.
[20] Borhanazad H, Mekhilef S, Ganapathy VG, Modiri-Delshad M, Mirtaheri A. Optimization of micro-grid system using MOPSO. Renew Energy 2014;71:295–306.
[21] Liu Y, Lu Y, Gao C, Zhang Z, Tao L. A multi-objective ant colony optimization algorithm based on the Physarum-inspired mathematical model. In: International conference on natural computation; 2014.
[22] Coello CAC, Pulido GT, Lechuga MS. Handling multiple objectives with particle swarm optimization. IEEE T Evolut Comput. 2004;8:256–79.
[23] Jeddi B, Einaddin AH, Kazemzadeh R. A novel multi-objective approach based on improved electromagnetism-like algorithm to solve optimal power flow problem considering the detailed model of thermal generators. Int T Ele Energy Syst 2016;27:1–20.
[24] Chen Z, Xia B, You C, Mi CC. A novel energy management method for series plug-in hybrid electric vehicles. Appl Energy 2015;145:172–9.
[25] Ali AM, Söffker D. Towards optimal power management of hybrid electric vehicles in real-time: a review on methods, challenges, and state-of-the-art solutions. Energies 2018;11(476):1–24.
[26] Song Z, Hofmann H, Li J, Hou J, Han X, Ouyang MJAE. Energy management strategies comparison for electric vehicles with hybrid energy storage system. App Energy 2014;134:321–31.
[27] Zhang S, Xiong R, Cao J. Battery durability and longevity based power management for plug-in hybrid electric vehicle with hybrid energy storage system. Appl Energy 2016;179:316–28.
[28] Veneri O, Capasso C, Patalano S. Experimental investigation into the effectiveness of a super-capacitor based hybrid energy storage system for urban commercial vehicles. Appl Energy 2017.
[29] Gruosso G. Model based design of power management for hybrid electric vehicle. In: 2015 IEEE 1st international forum on research and technologies for society and industry leveraging a better tomorrow (RTSI), Turin, Italy; 2015.
[30] Zhang S, Xiong R, Sun F. Model predictive control for power management in a plug-in hybrid electric vehicle with a hybrid energy storage system. Appl Energy 2017;185:1654–62.
[31] Feroldi D, Carignano M. Sizing for fuel cell/supercapacitor hybrid vehicles based on stochastic driving cycles. Appl Energy 2016;183:645–58.
[32] Paganelli G. Conception et commande d'une chaîne de traction pour véhicule hybride parallèle thermique et électrique.: Ph.D. dissertation, Université de Valenciennes, Valenciennes; 1999.
[33] Onori S, Serrao L, Rizzoni G. Hybrid electric vehicles. London: Springer; 2016.
[34] Paganelli G, Ercole G, Brahma A, Guezennec Y, Rizzoni G. General supervisory control policy for the energy optimization of charge-sustaining hybrid electric vehicles. JSAE Rev 2001;22:511–8.
[35] Onori SLS, Rizzoni G. Adaptive equivalent consumption minimization strategy for hybrid electric vehicles. In: Proceedings of the 2010 ASME dynamic systems and control conference; 2010.
[36] Fu L, zgüner ÜÖ, Tulpule P, Marano V. Real-time energy management and sensitivity study for hybrid electric vehicles. In: American control conference; 2011.
[37] Jing Wang YH, Xie H, Tian G. Driving pattern recognition and energy management for extended range electric bus. In: 2014 IEEE Vehicle power and propulsion conference (VPPC); 2014. p. 1–6.
[38] Holtrop J, Mennen GGJ. An Approximate power prediction method. Int Shipbuild Prog 1982;29:166–70.
[39] Carlton JS. Marine propellers and propulsion. 3rd ed.; 2012.
[40] Hou J, Sun J, Hofmann HF. Mitigating power fluctuations in electric ship propulsion with hybrid energy storage system: design and analysis. IEEE J Ocean Eng 2017;1–15.
[41] Zhao F, Yang W, Tan WW, Yu W, Yang J, Chou SK. Power management of vessel propulsion system for thrust efficiency and emissions mitigation. Appl Energy 2016;161:124–32.
[42] Bernitsas MMKT. KQ and efficiency curves for the. Wageningen B-Series Propell 1981.
[43] Rizzoni G, Guzzella L, Baumann BM. Unified modeling of hybrid electric vehicle drivetrains. IEEE-ASME T Mech 1999;4:246–57.
[44] Sorrentino M, Mauramati F, Arsie I, Cricchio A, Pianese C. Nesci W. Application of Willans line method for internal combustion engines scalability towards the design and optimization of eco-innovation solutions. International conference on engines & vehicles. 2015. p. 468–76.
[45] Wang B, Xu M, Li Y. Study on the economic and environmental benefits of different EV powertrain topologies. Energy Convers Manage 2014;86:916–26.
[46] Pisu P, Rizzoni G. A comparative study of supervisory control strategies for hybrid electric vehicles. IEEE T Contr Syst T 2007;15:506–18.
[47] Baldi F, Ahlgren F, Melino F, Gabrielii C, Andersson K. Optimal load allocation of complex ship power plants. Energy Convers Manage 2016;124:344–56.
[48] Divya KC, Østergaard J. Battery energy storage technology for power systems—an overview. Electr Pow Syst Res 2009;79:511–20.
[49] Chen BC, Wu YY, Tsai HC. Design and analysis of power management strategy for range extended electric vehicle using dynamic programming. Appl Energy 2014;113:1764–74.
[50] Johnson VH. Battery performance models in ADVISOR. J Power Sources 2002;110:321–9.
[51] Askarzadeh A. Distribution generation by photovoltaic and diesel generator systems: energy management and size optimization by a new approach for a stand-alone application. Energy 2017;122:542–51.
[52] Dufo-López R, Bernal-Agustín JL, Mendoza F. Design and economical analysis of hybrid PV–wind systems connected to the grid for the intermittent production of hydrogen. Energ Policy 2009;37:3082–95.
[53] Diesel-electric Propulsion Plants: A brief guideline how to engineer a diesel-electric propulsion system. [Online]. Available: http://marine.man.eu. last visited 9.2015. Man Diesel; 2015.
[54] Azaza M, Wallin F. Multi objective particle swarm optimization of hybrid micro-grid system: a case study in Sweden. Energy 2017;123:108–18.
[55] Musardo C, Rizzoni G, Guezennec Y, Staccia B. A-ECMS: an adaptive algorithm for hybrid electric vehicle energy management. Eur J Control 2005;11:509–24.
[56] Ahmadi MH, Ahmadi MA, Sadatsakkak SA. Thermodynamic analysis and performance optimization of irreversible Carnot refrigerator by using multi-objective evolutionary algorithms (MOEAs). Renew Sust Energ Rev 2015;51:1055–70.
[57] Olson DL. Comparison of weights in TOPSIS models. Math Comput Modell 2004;40:721–7.
[58] Sciberras EA, Zahawi B, Atkinson DJ, Juandó A. Electric auxiliary propulsion for improved fuel efficiency and reduced emissions. Proc Inst Mech Eng, Part M: J Eng Maritime Environ 2015;229:36–44.
[59] Hung YH, Tung YM, Chang CH. Optimal control of integrated energy management/mode switch timing in a three-power-source hybrid powertrain. Appl Energy 2016;173:184–96.
[60] Zahedi B, Norum LE, Ludvigsen KB. Optimized efficiency of all-electric ships by dc hybrid power systems. J Power Sources 2014;255:341–54.
[61] Donateo T, Licci F, D'Elia A, Colangelo G, Laforgia D, Ciancarelli F. Evaluation of emissions of CO2 and air pollutants from electric vehicles in Italian cities. Appl Energy 2015;157:675–87.
[62] Offshore SP. M/V Pacific Valhalla [Online]. Available: https://www.swirespo.com/. last visited 9.2015. Swire Pacific Offshore Operations (Pte) Ltd.; 2017.
[63] Sandmo T. The Norwegian Emission Inventory 2011: documentation of methodologies for estimating emissions og greenhouse gases and long-range transboundary air pollutants. J Phys Chem 2011;115:10069–77.
[64] Edwards R, Mahieu V, Griesemann J-C, Larivé J-F, Rickeard DJ. Well-to-wheels analysis of future automotive fuels and powertrains in the European context. SAE Trans 2004.
[65] Doucette RT, Mcculloch MD. Modeling the CO2 emissions from battery electric vehicles given the power generation mixes of different countries. Energy Policy 2011;39:803–11.
[66] Dinu O, Ilie AM. Maritime vessel obsolescence, life cycle cost and design service life. Modern Technol Industr Eng 2015;95:12–67.
[67] Lan H, Wen S, Hong YY, Yu DC, Zhang L. Optimal sizing of hybrid PV/diesel/battery in ship power system. Appl Energy 2015;158:26–34.
[68] Ådnanes AK. Maritime electrical installations and diesel electric propulsion. Abb As Marine. 2003.